Atmospheric Environment 52 (2012) 121–130

Contents lists available at SciVerse ScienceDirect

Atmospheric Environment

journal homepage: www.elsevier.com/locate/atmosenv

Taking the pulse of pyrocumulus clouds

C.K. Gatebe [a,b,*], T. Varnai [b,c], R. Poudyal [b,d], C. Ichoku [b], M.D. King [e]

[a] Universities Space Research Association, Columbia, MD 21228, USA
[b] NASA Goddard Space Flight Center, Greenbelt, MD 20771, USA
[c] University of Maryland, Baltimore County, Baltimore, MD 21228, USA
[d] Science Systems and Applications, Inc., Lanham, MD 20706, USA
[e] Laboratory for Atmospheric and Space Physics, University of Colorado, Boulder, CO, USA

ARTICLE INFO

Article history:
Received 14 October 2011
Received in revised form
19 January 2012
Accepted 20 January 2012

Keywords:
Remote sensing
Pyrocumulus
Clouds
Smoke
Fires
Biomass burning
Radiometer
Monte Carlo
Three-dimensional (3D) radiative transfer
Diffusion approximations
Airborne
CAR
NASA P-3B

ABSTRACT

Large forest fires are a known natural and dominant disturbance factor in high northern latitudes, and form pyrocumulus (pyroCu), and occasionally pyrocumulonimbus (pyroCb) clouds. These clouds can transport emissions into the upper troposphere/lower stratosphere (UT/LS) and produce significant regional and even global climate effects, as is the case with some volcanoes. However, the lack of observational data within pyroCu or pyroCb complicates our ability to investigate pyro-convection and to understand the vertical and cross-isentropic transport mechanisms responsible for UT/LS injection. Here, we report detailed airborne radiation measurements within strong pyroCu taken over boreal forest fires in Saskatchewan, Canada during the Arctic Research of the Composition of the Troposphere from Aircraft and Satellites (ARCTAS) summer field campaign in 2008. We find a prominent smoke core within the pyroCu, which is defined by strong extinction in the UV, VIS and NIR, and high gas-particle concentrations. We also find that the angular distribution of radiance within the pyroCu is closely related to the diffusion domain in water clouds, which is dominated by multiple scattering processes. The radiation field of pyroCu can be described by diffusion approximations that are comprised of simple cosine functions, which can be used to calculate the spatial and temporal characteristics of the radiance field, and applied in cloud resolving models. We demonstrate with Monte Carlo simulations that radiation transport in pyroCu is inherently a 3D problem and must account for particle absorption.

1. Introduction

Large forest fires can produce pyrocumulus (pyroCu) or pyrocumulonimbus (pyroCb) and can transport smoke pollutants into the upper troposphere/lower stratosphere (UT/LS) as documented in many studies (e.g. Fromm et al., 2005; Fromm and Servranckx, 2003). The transport of smoke from the boundary layer to the free troposphere can be seen as transforming a local air pollution problem into a regional or global problem (Damoah et al., 2006; Luderer et al., 2006; Trentmann et al., 2006; Donnell et al., 2001). Fires of this nature are common in summer in the boreal regions of Alaska, Canada, and Russia (Fromm et al., 2010; Soja et al., 2007; Stocks et al., 2003), and can perturb regional, and probably global radiation budgets by their light-scattering effects and by their influence on cloud microphysical processes (Andreae et al., 2004). There is now growing evidence that wildfires should be considered as additional sources of aerosol and trace gases to the UT/LS region, which was previously thought to be primarily dominated by volcanic eruptions (Fromm et al., 2010; Luderer et al., 2006).

Large forest fires release enough energy, both sensible and latent heat, to lift the smoke-laden air beyond the condensation level, resulting in the formation of cumulus clouds. There is still significant uncertainty on how much of the energy released by combustion contributes to local heating of the atmosphere and is available for convection, and how much of the energy is lost due to radiative processes. Commonly found estimates for the radiative energy are between nearly 14% (Wooster et al., 2005) and 50% (McCarter and Broido, 1965; Packham, 1969). These estimates are based on laboratory studies or observations of small-scale fires, and their application to large-scale crown fires resulting in pyroCu or pyroCb convection is subject to considerable uncertainty. The interaction of this radiative energy with atmospheric constituents is also highly uncertain. In the thermal infrared, where most of the

* Corresponding author. Universities Space Research Association, Columbia, MD 21228, USA.
E-mail address: charles.k.gatebe@nasa.gov (C.K. Gatebe).

1352-2310/$ – see front matter © 2012 Elsevier Ltd. All rights reserved.
doi:10.1016/j.atmosenv.2012.01.045

fire radiation is emitted (Wooster, 2002), aerosols are rather inefficient absorbers. It is likely that most of the radiative energy from the fire is absorbed by cloud droplets or gaseous absorption at cloud base or in air masses that are entrained into the convective plume. This implies that the radiative energy from the fire is trapped in the lower part of the pyro-convection and therefore contributes to the convective energy. It is therefore important to consider the radiative processes in pyroCu in detail.

The assessment of the radiative processes of optically dense media such as pyroCu, which are dominated by multiple light scattering and absorption is a daunting task, and requires a solution of the three-dimensional (3D) radiative transfer equation. However, a number of approximations have been developed which provide efficient and reasonably accurate solutions of the radiative transfer equation, if some necessary conditions are fulfilled (Polonsky and Davis, 2004). For the case of optically dense weakly absorbing media, such as water-droplet clouds, it has been shown that the framework of the diffusion approximation (DA) can be used (Polonsky and Davis, 2004). The simplicity of this type of approach allows derivation of an analytical solution for the forward problems, such as simulation of radiance characteristics in 3D cloud optics.

However, a major challenge in developing such diffusion approximations for pyroCu or realistic fire plume models is the lack of observational data on smoke within forest fire plumes that can be used for validating these models. This is not a big surprise, because making observations within forest fire plumes is challenging at best, and flying into the "core" of rising smoke can be very risky. The possibility of damaging expensive instrumentation is also high. Here, we report detailed radiation measurements from within a pyroCu core taken onboard the NASA P-3B aircraft during the Arctic Research of the Composition of the Troposphere from Aircraft and Satellites (ARCTAS) experiment, which took place in Canada in June–July 2008 (Jacob et al., 2010). Such measurements are needed in the investigations of pyro-convection on the spatial scale of individual events, i.e., tens of meters to a few hundred meters. This would contribute to the understanding of the vertical and cross-isentropic (quasi-vertical) transport mechanisms responsible for high-altitude tropospheric and stratospheric injection (Luderer et al., 2006). These radiation measurements are unique and we are not aware of any previous radiation measurements within a forest fire plume at the scales described in the next section.

This study focuses on 2 July 2008 and 6 July 2008, the fourth and sixth flights of the P-3B, respectively, out of Cold Lake, Canada during ARCTAS. These flights provided opportunities for in situ observations of flaming fires, plume evolution and vertical profiles of plumes in homogeneous fire outflow regions. Most importantly, they are the only flights where the P-3B penetrated the pyroCu clouds of active fire plumes. In this study, we emphasize data obtained with a multi-wavelength scanning radiometer, NASA's Cloud Absorption Radiometer (CAR; Gatebe et al., 2003; King et al., 1986), which provides unprecedented detail on pyroCu clouds.

The CAR instrument measures scattered light in 14 spectral bands between 0.34 and 2.30 μm, and has a unique scanning geometry. The CAR scan mirror scans 360° in a plane perpendicular to the direction of flight and the data are collected through a 190° field of view (1° instantaneous field of view; Fig. 1). When it is flown inside clouds, it is able to provide a side view in the zenith and nadir directions, and all scattering angles in between from an aircraft platform. Data are sampled simultaneously and continuously on nine individual detectors. Eight of the data channels for spectral bands from 0.34 to 1.27 μm are always registered during the operation, while the ninth data channel is registered for signal selected among six spectral channels (1.55–2.30 μm) on a filter wheel. The filter wheel can either cycle through all six spectral bands at a prescribed interval (usually changing filter every fifth scan line), or lock onto any one of the six spectral bands, mostly 1.656, 2.103, or 2.205 μm, and sample it continuously.

2. Observational assessment of the pyroCu

Some of the biggest Saskatchewan fires during the 2008 summer ARCTAS campaign burned west of Mcintosh Lake and east of Lake Athabaska in Canada. On 2 July (P-3 Flight #18/CAR Flight # 2017) and 6 July (P-3 Flight #20/CAR Flight # 2019) the conditions for fires seemed right, as a cold front moved over the region setting up conditions conducive to sending hot smoke plumes billowing into the upper atmosphere. The P-3B aircraft, with its suite of instruments, was in the air and managed to acquire very good fire data. Below, we provide a general description of the 2 July flight and the primary instruments that were operating during the flight. We will not describe the 6 July flight because of similarities between the two flights, however, full details for this flight can be found on the CAR website (http://car.gsfc.nasa.gov/data/index.php?id=115&mis_id=8&n=ARCTAS). Through these descriptions, we attempt to paint a picture of the nature and character of the fires and in addition, create a preamble for further work on pyroCu and their effects on climate.

2.1. NASA P-3B payload during ARCTAS 2008

Fig. 1a shows the platform we used in this campaign, the NASA P-3B aircraft. The picture was taken at NASA Ames on 24 June 2008 just before a transit flight to Cold Lake, Canada at the start of the ARCTAS summer campaign. The P-3B payload included 10 primary instruments (see Table 1) for measuring aerosol optical depth, aerosol extinction and scattering, aerosol size distribution (Russell et al., 1999; Clarke et al., 2007), solar spectral (0.380–2.200 μm) downwelling and upwelling irradiance (Pilewskie et al., 2003), broadband downwelling and upwelling solar (0.2–3.6 μm) and IR (4.5–42 μm) irradiance (A. Bucholtz personal communication: http://airbornescience.nasa.gov/instrument/BBR), angular distribution of scattered radiation in different directions (Gatebe et al., 2003), cloud condensation nuclei (Roberts and Nenes, 2005; Lance et al., 2006), and NO_2 and carbon monoxide (Strawa et al., 2007; Provencal et al., 2005). The base meteorological and navigational measurements were provided by the Project Data System, which is the primary navigational data system for P-3B investigators (Barrick and Aknan, 2008).

Fig. 1b shows a schematic of the CAR instrument (Gatebe et al., 2003; King et al., 1986), highlighting its main features. Fig. 1c shows a pyroCu taken onboard the NASA P-3B on 2 July 2008 near Reindeer Lake, Saskatchewan, Canada. The aircraft flew around these fires, sampling clean air upwind and the polluted air downwind. It then flew through the smoke at various altitudes, probing and charting changes in concentration and the "chemical evolution" of the compounds emitted by the fires. The aircraft also flew into the "core" of the rising fire plumes, where the CAR instrument managed to acquire good data as discussed in this study. These represent the first such measurements in the core of a pyroCb of which we are aware. (See pictures from the 2 July flight on the CAR website at http://car.gsfc.nasa.gov/data/photos.php?mis_id=8&n=ARCTAS&d=2008-07-02&f=2017&l=h and from the 6 July flight at http://car.gsfc.nasa.gov/data/photos.php?mis_id=8&n=ARCTAS&d=2008-07-06&f=2019&l=h).

2.2. Description of flight 2017, 2 July 2008

Our objectives for this flight included flying a segment under the Terra satellite, coordinated with the NASA B-200

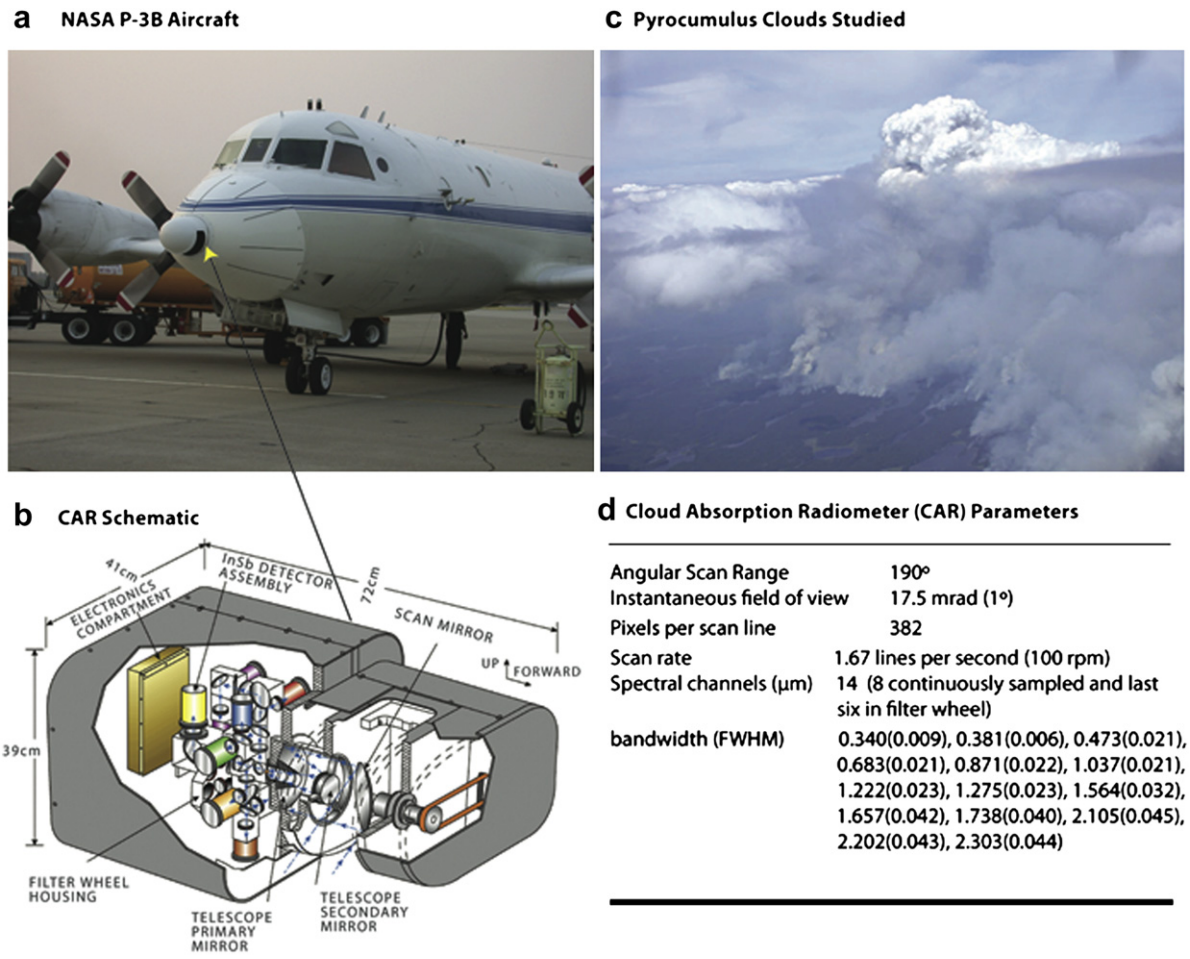

Fig. 1. (a). The NASA P-3B at NASA Ames Research Center, California, USA in June 2008 during the ARCTAS field experiment. (b) Schematic of NASA's Cloud Absorption Radiometer (CAR), which is mounted in the nose of the NASA P-3B aircraft. (c) Picture of the fire plume that the P-3 penetrated on 2 July during ARCTAS. (d) Specifications for the CAR, which contains 14 narrow spectral bands between 0.34 and 2.30 μm. The CAR flew nine fire missions aboard P-3B in Canada between 28 June and 10 July 2008.

carrying the High Spectral Resolution Lidar (HSRL) and the Research Scanning Polarimeter (RSP) with radiation measurements under clear sky conditions stacked at different altitudes, and in situ observations of flaming fires, showing plume evolution and vertical profiles in homogeneous fire outflow regions. The flight took 6 h and 20 min, with take off at 15:31 UTC (9:31 a.m. local time; see flight log: http://car.gsfc.nasa.gov/data/index.php?id=113&mis_id=8&n=ARCTAS). Fig. 2a shows the flight path from Cold Lake, heading northeast towards Reindeer Lake. We made measurements collocated with the B-200 for about 50 min beginning at 16:25 UTC, and observed active fires of different intensities under scattered cloud conditions. We penetrated an active fire plume near Mcintosh Lake at two altitudes, 1303 m (19:18 UTC) and 294 m (19:49 UTC) above the local surface, and flew along the plume axis for about 80 km to study the evolution of aerosol microphysics during downwind transport. Between the two penetrations, we obtained radiation measurements in a vertical profile in the most homogeneous part of the plume and flew across-plume at a low level. We also sampled outflow from a pyroCu cloud and penetrated the cloud to sample the inside. Fig. 2b shows an image taken by the Moderate Resolution Imaging Spectroradiometer (MODIS) flying aboard the Aqua satellite at 19:35 UTC over the region highlighted in the white box in Fig. 2a. The cloud fields seen in the satellite image are most likely associated with the active fires in the region. Note that the green squares represent fire locations detected by MODIS on the Terra satellite taken during the overpass earlier that day, at 17:55 UTC. The red squares represent fire locations as seen with the MODIS/Aqua 4-μm channel during the overpass (e.g. Giglio et al., 2003) at 19:35 UTC. The orange square marks the location of the fire plume that was penetrated by the P-3B at 21:04 UTC.

Fig. 2c and d show CAR quick-look images selected from a section of the flight where the aircraft went through a pyroCu core during the flight of 2 July (the green line in Fig. 2b highlights the flight path through the pyroCu). A combination of different CAR bands representing red, green, and blue colors helps to differentiate between clouds and smoke and to see through smoke, revealing land surface features such as green vegetation and dark water bodies (see Fig. 2c: false-color RGB (0.47, 0.38, 0.34) μm; Fig. 2d: false-color RGB (1.66, 1.04, 0.38) μm). As shown in Fig. 2d, the fire was widespread, covering hundreds of hectares, and it took the aircraft ~15 s to cross the core (the central core covers a ground area ~2 km (cf. Fig. 3), where the measured aircraft groundspeed varied between 127 ms^{-1} and 138 ms^{-1}). The aircraft altitude changed dramatically while traversing the core, rising by 93 m, from 2747 m to 2840 m above mean sea level (msl), an indication of strong updrafts >8 ms^{-1}.

The height of the 2 July pyroCu top above ground was >3000 m, and the boundary layer (BL) height at the fire location and time of aircraft data acquisition was 1976 m. The BL was obtained by interpolating the values for 12 noon and 3 pm local times from the NASA Goddard Earth Observing System (GEOS-5) data provided by

Table 1
P-3B Aircraft Instrumentation for ARCTAS.

Instrument name	Data products	Technique	Principal investigator	Detection limit (Nominal accuracy)
AERO3X	Aerosol optical properties, NO_2 mixing ratio	Cavity ring-down extinction; Sample rate: 2 s (Strawa et al., 2007).	A. Strawa, NASA ARC	Extinction and scattering – 2 σ sensitivity ≈ 0.2 Mm^{-1}, Extinction and scattering – 2 σ precision ≈ 0.1 Mm^{-1}, NO_2 mixing ratio – 2 σ sensitivity better than 1 ppb
Ames Airborne Tracking Sunphotometer (AATS)	Aerosol optical depth and extinction, water vapor column and profile	Tracking Sun photometer, 0.354–2.138 μm (Russell et al., 1999)	J. Redemann, BAERI/NASA ARC	Slant OD ~0.002 (±0.01) Slant WV ~0.0005–0.006 gcm^{-2} (±8%)
Broad Band Radiometers (BBR)	Radiation fluxes (solar: 0.2–3.6 μm & IR: 4.5–42 μm)	Radiometer	A. Bucholtz, NRL	Estimated Accuracy: 3–5%
Cloud Absorption Radiometer (CAR)	Radiance, aerosol, cloud & Earth surface properties	Angular (cross-track zenith to nadir) scanning radiometer, 0.340–2.301 μm	C. Gatebe, USRA/NASA GSFC	Radiance absolute accuracy <5%
Continuous-Flow Streamwise Thermal Gradient Cloud Condensation Nuclei (CCN) Counter (CFSTGC)	Cloud Condensation Nuclei (CCN)	Supersaturation generated by relative diffusion of water vapor and heat (Roberts and Nenes, 2005)	A. Nenes, Georgia Tech	SS Range: 0.20–0.60%, ±0.05%
Carbon monoxide By Attenuated Laser Transmission (COBALT)	CO mixing ratio (mole fraction) at a 1-Hz rate based on measured absorption, gas temperature, and pressure using Beer's Law	Off-axis integrated cavity output spectroscopy–TLAS (Provencal et al., 2005)	J. Podolske, NASA/ARC	Precision: 0.2 ppbv (1-s averaging time), uncertainty <1.0%
Hawaii Group for Environmental Aerosol Research (HiGEAR)	Aerosols (Aerosol number, size, composition, volatility, optical properties; Clarke et al., 2007; Shinozuka et al., 2011; Howell et al., 2006)	OPC, PSAP, TDMA, CN counter, ToF-AMS, SP2, nephelometer	A. Clarke, U. Hawaii	See references: Shinozuka et al. (2011).
Project Data System (PDS)	Base meteorological (P, T, RH) and navigational measurements	See reference: Barrick	John Barrick NASA/LaRC	See references: Barrick
Solar Spectral Flux Radiometer (SSFR)	Solar spectral flux	Spectrometer (380–1700 nm) with nadir and zenith hemispheric collectors	S. Schmidt, U. Colorado	Absolute accuracy 3–5%. Precision 1%

the Global Modelling and Assimilation Office (GMAO). Therefore, the pyroCu extended well above the boundary layer. Recent studies based on digitized plume height analysis from the Multi-angle Imaging SpectroRadiometer (MISR) instrument aboard the Terra satellite have shown that of order 10% of the plumes are injected higher than 0.5 km above the BL; out of eight North American biome types evaluated, fire plumes from boreal forests (which include the study area) are typically injected the highest, with a median injection top height of ~1200 m (as compared to ~800 m for croplands; Kahn et al., 2008; Val Martin et al., 2010). Those studies also found a correlation between the plume injection height and fire radiative power (FRP) measurements from MODIS (Ichoku et al., 2008), indicating that in addition to atmospheric stability structure, fire intensity (represented by FRP) has a strong influence on plume injection height; plume top heights that reached the free troposphere (FT) were produced mainly by high intensity fires having a median FRP of order 500 MW. Table 2 shows the FRP values of the MODIS fire pixels (depicting their single-pixel relative intensities) from Aqua coinciding with 2 July 2008 flight (in space but not in time). The FRP data record corresponding spatially to the pyroCu plume penetrated by P-3B is shown in boldface characters. The FRPs recorded by MODIS (e.g. Aqua-MODIS, 19:35 UTC) are too low to account for the pyro-convective activity observed during P-3B penetration of the pyroCu at about 21:05 UTC. This could be for a number of reasons which include: 1) uncertainties in single-pixel FRP retrievals are extremely high (cf. Calle et al., 2009), and 2) vigorous burning coupled with convective activity can result in clouds which are partly or completely opaque at 4 μm, which obscures fire detection (cf. Csiszar et al., 2006). The 90-min difference in overpass can also play a role, as pyro-convection can evolve very quickly in Canada (cf. Rosenfeld et al., 2007). For the P-3B pyroCu penetration on 6 July 2008, no fire pixels were detected by MODIS within a few km of the pyroCu. It is believed that the pyroCu may have moved substantially away from the fire at the time of its penetration, making it impossible to link it to any specific fire detected by MODIS. Therefore, to establish a cause and effect relationship of such transient features as fires and their associated plumes and pyroCu, it is crucial to conduct airborne measurements in synchronicity with satellite overpasses and ground-based measurements whenever possible.

In the next section, we will discuss the CAR measurements inside pyroCu and results from a Monte Carlo simulation of the radiation field within optically dense media analogous to those observed above.

3. Results and discussion

3.1. Analysis of CAR measurements

The core of the pyroCu as seen in Fig. 2c and d stands out as a very dark region of the plume, where radiation seems to be uniformly distributed and dominated by strong absorption in all directions. The CAR instrument measured very low spectral radiance values (<1 Wm^{-2} μm^{-1} sr^{-1} in the ultraviolet and visible bands having $\lambda < 0.5$ μm, and at $\lambda = 1.6$ μm, and 2–5 Wm^{-2} μm^{-1} sr^{-1} for bands between 0.5 μm and 1.3 μm; cf. Table 3), independent of direction. The radiance distributions within the core at two zenith angles: 5° and 175° at 0.472 μm, shown in Fig. 3 demonstrate that there is hardly any difference between the downwelling and upwelling radiance within the core region. The a, b and c images in this figure were taken by a forward camera aboard the NASA P-3B at the entry, core, and exit points in the pyroCu. Note the brownish color of the plume inside the core region. The radiance decreases by about two orders of magnitude from outside to the central part of the core, irrespective of the

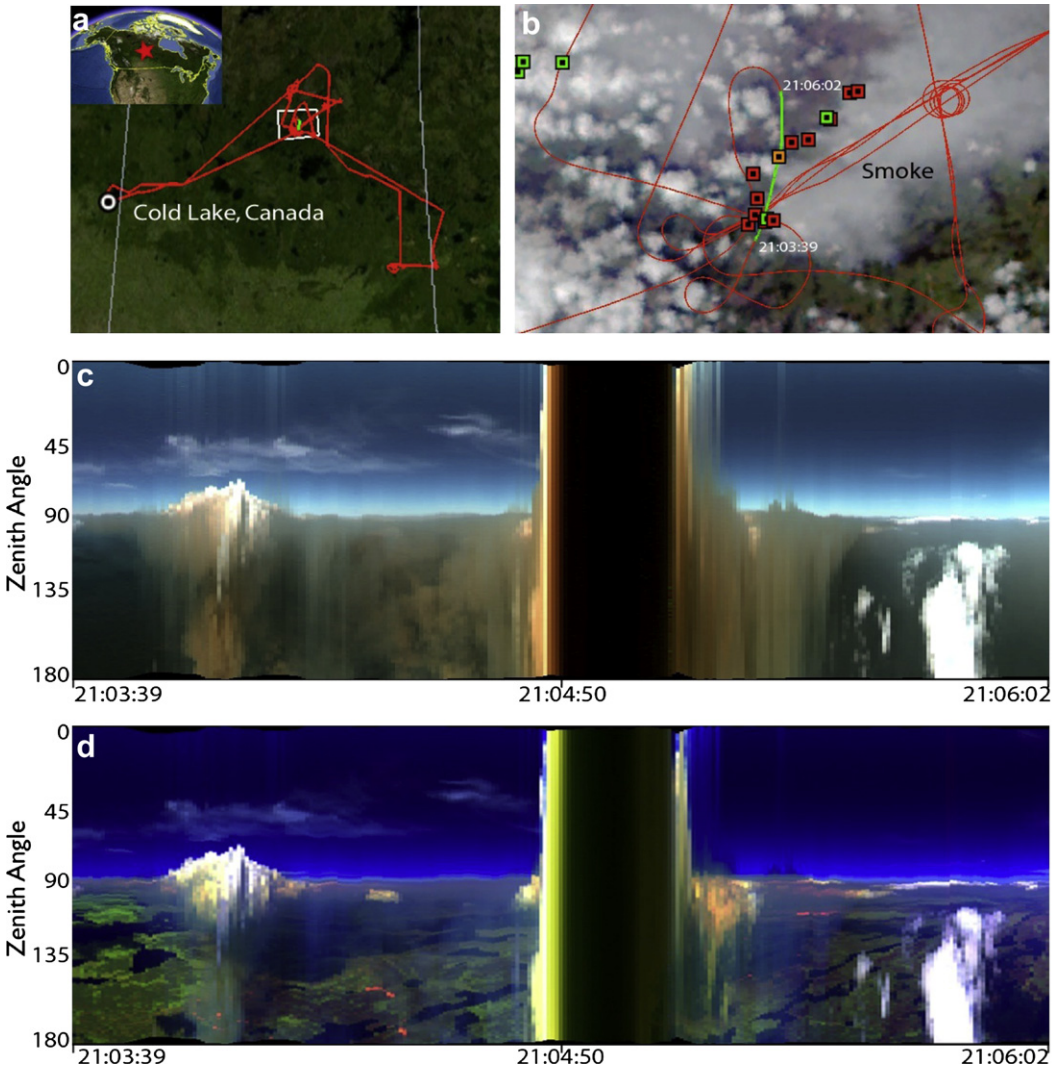

Fig. 2. (a) NASA P-3B flight track on 2 July 2008 during the ARCTAS 2008 summer campaign. (b) MODIS/Aqua image taken on 2 July 2008 over the area marked by the rectangle in (a). The green (red) squares are fire locations during Terra (Aqua) overpass at 17:55 UTC (19:35 UTC), and the orange square marks the location of the fire plume that was penetrated by the P-3B. (c)–(d) CAR quick-look images of the fires taken aboard the NASA P-3B over the flight section highlighted in green in (b). A combination of red, green, and blue colors using different CAR bands helps differentiate cloud from smoke, and to see through smoke and identify land surface features such as green vegetation and dark water bodies. The red, green, and blue color assignments in (c) are 0.47, 0.38, 0.34 μm and for (d) 1.66, 1.04, 0.38 μm.

direction and wavelength. Given these radiation characteristics, the strength of the updraft, and the fact that CO concentrations (and cloud condensation nuclei, CCN) were highest in the core region (J. Podolske and A. Nenes personal communication), we speculate that the core region plays an important role as a pathway through which heat and emissions from fires are transported to the upper levels in the atmosphere. But this hypothesis needs to be validated.

Fig. 4 compares relative spectral radiance (or spectral radiance ratio: $I_\lambda(\theta, \varphi)/I_\lambda(\theta^*, \varphi)$, where θ^* is the zenith angle of maximum spectral radiance – cf. Table 3) as a function of zenith angle for internally scattered radiation measured deep inside (a) an optically thick water cloud, (b) pyroCu, (c) pyroCu core and (d) a thick "pure" smoke, which is defined by lack of reflectance sensitivity in the near-infrared bands ($\lambda \geq 0.87$ μm), at selected CAR wavelengths. According to King et al. (1990), radiance measurements from an individual scan of the CAR inside an optically thick water cloud are considered to be in the diffusion domain, if three conditions are satisfied: (i) the zenith radiance exceeds the nadir radiance, (ii) the maximum deviation from the theoretical cosine curve is less than or equal to 5% of the mean amplitude, and (iii) the number of times the deviations from a cosine distribution changes sign is greater than or equal to 4, which helps to assure that fluctuations are random, and not systematic drifts. These criteria pertain to the diffusion domain of an optically thick media if the scattering is conservative (no absorption), and thus are to be expected for liquid water clouds at wavelengths around 0.67 μm (as seen in Fig. 4a). The theoretical curve is generated from measured zenith and nadir radiances using the following cosine relationship

$$I(\tau, \cos\theta) = a + b\cos\theta \tag{1}$$

where

$$a = \frac{1}{2}(I_0(\tau, 1) + I_{180}(\tau, -1)),$$
$$b = \frac{1}{2}(I_0(\tau, 1) - I_{180}(\tau, -1)) \tag{1a}$$

and I_0 and I_{180} are the zenith and nadir radiances at $\theta = 0^\circ$ and $\theta = 180^\circ$, respectively. From Eq. (1a), we came up with a general

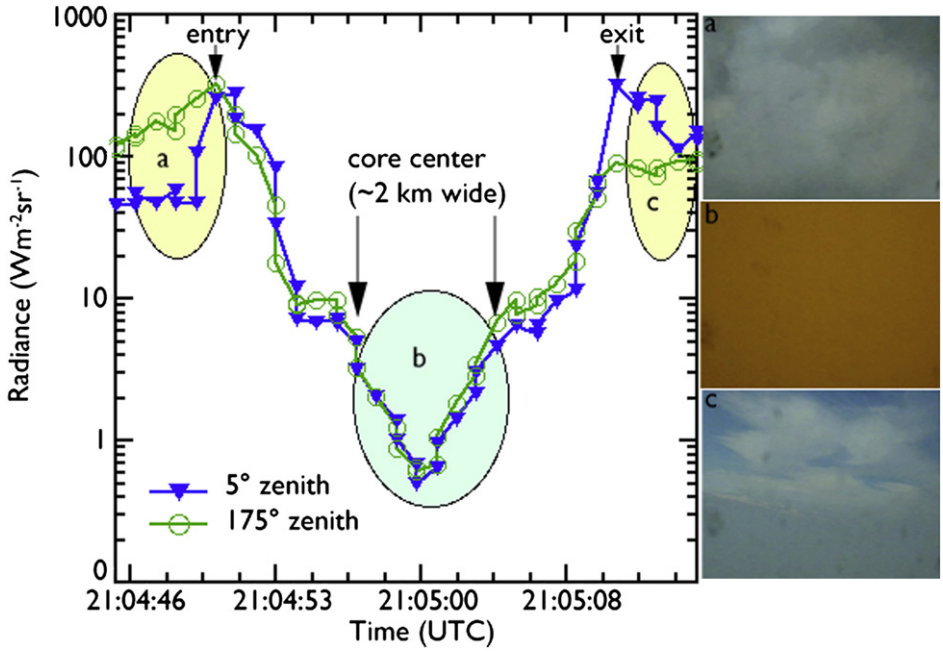

Fig. 3. Zenith and nadir radiances at 0.472 μm, on a flight through a pyroCu (cf. Fig. 2c–d), between 21:04:45 and 21:05:29 UTC, on 02 July 2008. Pictures a, b and c are from a forward camera aboard the NASA P-3B, and coincide with entry, core penetration, and exit points of the pyroCu, respectively. The core was very dark, and brownish in color, with strong updrafts (>8 ms^{-1}). The distance from the core to the edge of the pyroCu is about 318 m. Flight level was ~2794 m msl.

equation for any two downward and upward viewing angles in the form

$$a = \frac{1}{2}\left(I_{\theta'}(\tau, \cos\theta') + I_{180-\theta'}(\tau, -\cos\theta')\right)$$
$$b = \frac{1}{2\cos\theta'}\left(I_{\theta'}(\tau, \cos\theta') - I_{180-\theta'}(\tau, -\cos\theta')\right) \quad (1b)$$

As such, Eq. (1b) is not restricted to using zenith ($\theta = \theta' = 0°$) and nadir ($\theta = \theta' = 180°$) input radiances, unlike Eq. (1a), and can be used to describe the radiation field in optically thick media given any two downward and upward zenith directions, or a combination of $\theta' = 90°$ (where $b = I_{90}(\tau)$) and any other direction. This general formula can be applied to CAR observations away from the zenith and nadir directions, and therefore can accommodate the realities of data acquisition on an airborne platform that has a nonzero pitch and/or roll angle. This makes it possible to apply Eq. (1) to real data, for example to determine whether the diffusion approximation (and hence diffusion-based models) can be used in analysing some observations.

Table 2
Locations and FRP values of fire pixels detected by Aqua-MODIS on 2 July 2008 at 19:35 UTC in the vicinity of the measured pyroCu, as indicated in Fig. 1b. The bold FRP values correspond spatially to the pyroCu plume penetrated by P-3B.

Latitude (°N)	Longitude (°W)	Fire radiative power (MW)
55.685	105.283	108.273
55.682	105.299	112.081
55.677	105.331	37.455
55.688	105.320	84.818
55.706	**105.320**	**105.710**
55.733	105.334	20.674
55.778	105.235	24.367
55.773	105.267	18.737
55.803	105.197	84.151
55.838	105.150	25.296
55.835	105.166	17.619

For the liquid water cloud case (Fig. 4a), obtained on 29 June 2008 (20:00 UTC) in Canada, the angular radiance field at the shortest wavelengths can be described by a cosine function expected for conservative scattering in the diffusion domain (King, 1981; King et al., 1990), where the cloud is expected to have a small to negligible amount of absorption. This is demonstrated in Fig. 5 (liquid water cloud case), where the angular distribution of the radiation field obtained from measurements (continuous curve, abstracted from Fig. 4a) is compared to that expected in the diffusion domain for conservative scattering (dotted curve) at $\lambda = 0.472$ μm. We note that the angular radiance field becomes increasingly anisotropic as absorption increases in the CAR bands at wavelengths exceeding 1 μm (Fig. 4a), because stronger absorption implies that a smaller portion of downwelling solar radiation can be reflected back up from below. In the water cloud case, the three conditions for the diffusion domain at a conservative scattering wavelength were met. King et al. (1990) show that when the three conditions are assured, quantitative information about cloud absorption properties from the angular distribution of scattered radiation can be derived, dependent only on the optical properties of the medium and possibly on the reflectivity of the underlying surface, but independent of the solar zenith angle and solar irradiance.

Table 3
Peak spectral radiance measured inside optically dense media (cf. Fig. 4).

Wavelength (μm)	Peak radiance (Wm^{-2} μm^{-1} sr^{-1})			
	Water cloud	pyroCu	pyroCu (core)	Smoke
0.340	71.13	1.40	0.24	29.98
0.380	107.12	4.11	1.34	68.06
0.473	184.99	8.41	5.50	189.07
0.683	129.53	6.40	11.84	156.34
0.871	88.06	6.13	13.58	90.95
1.036	56.02	4.34	11.64	52.04
1.222	21.10	2.01	7.16	26.30
1.275	19.28	1.81	6.77	21.31

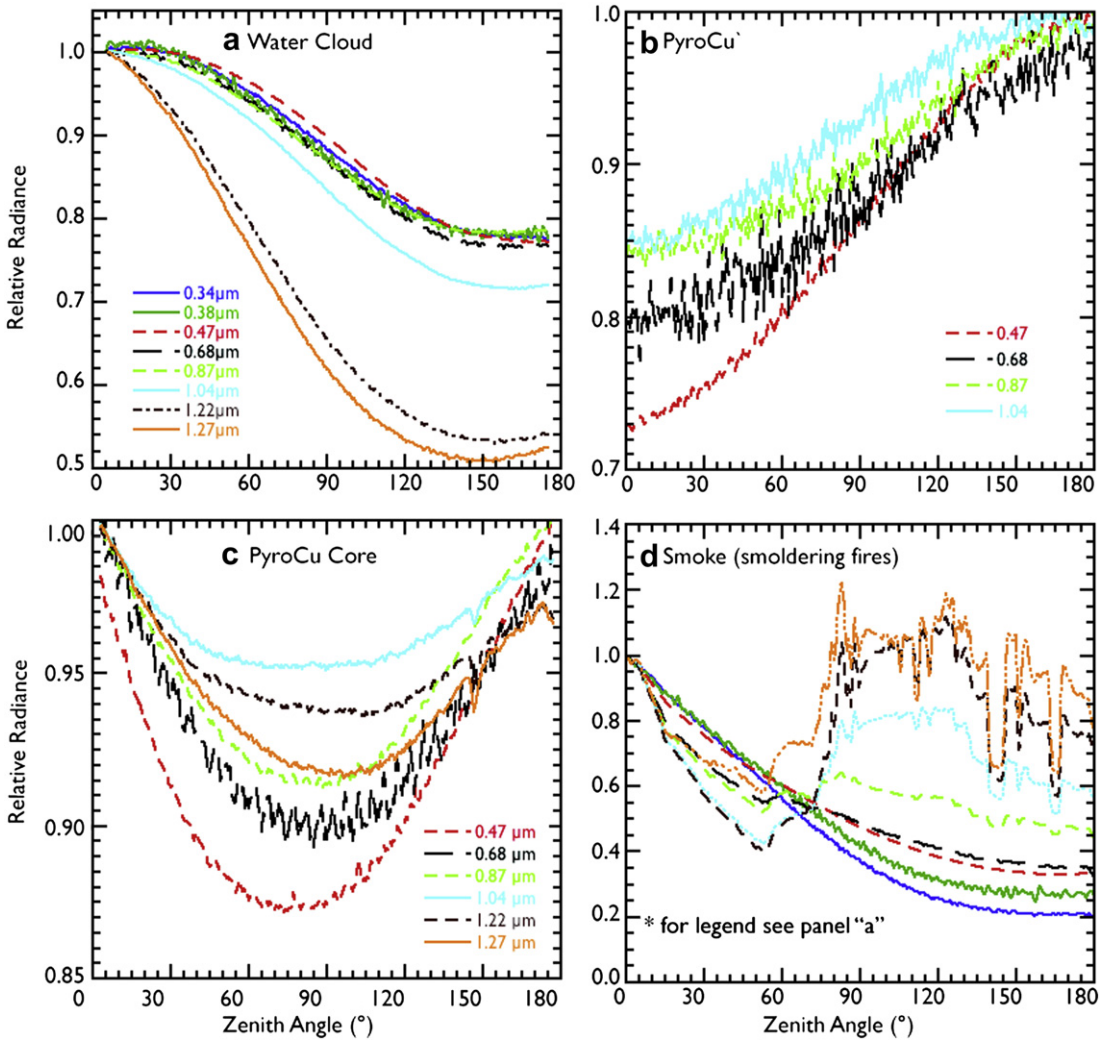

Fig. 4. Relative spectral radiance ($I_\lambda(\theta, \varphi)/I_\lambda(\theta^*, \varphi)$) from CAR, where θ^* is the zenith angle of maximum/peak spectral radiance (cf. Table 3), as a function of zenith angle for internally scattered radiation measured in Canada during ARCTAS inside (a) liquid water cloud, 29 June, (b) pyroCu, 6 July, (c) core of pyroCu, 2 July, and (d) thick smoke from smoldering fires with no cloud present, 10 July. The UV channels are not included in (b) and (c) because of low signal-to-noise values. The effects of surface reflectance are clearly seen in the "pure smoke" case (d) at wavelengths, $\lambda \geq 0.68$ μm.

The problem now is to describe the radiation pattern inside an optically thick pyroCu, the core of a pyrcoCu, and smoke, which seem to be increasingly anisotropic as absorption tends to dominate at the shorter wavelength and is not negligible. However, the diffusion domain theory for optically thick clouds with modified a and b (Eq. (1b); Fig. 4b), can also describe the angular radiance distribution in a pyroCu as shown in Fig. 5 (blue solid curve represents measurements, green dotted line represents the fit), but b must assume a negative value, because in this case, the relative radiance is highest at nadir rather than at zenith. The cosine function can also represent the pyroCu core case (Fig. 4c), but an additional term is needed (Eq. (2)) to reproduce the bowl shaped curves in Figs. 4c and 5 (note that the solid lines represent observations, while dotted lines represent fit to the observations). While in principle the new term could involve a second cosine or some other function, we found that a sine term provides the best fit to our data (especially near nadir and zenith), yielding:

$$I(\tau, \cos\theta) = (a + b\cos\theta) + (c + d\sin\theta) \quad (2)$$

The parameters a and b are easily determined from Eq. (1b). The last two terms represent a mathematical ansatz, where the term c is obtained from zenith and nadir radiances following the same principle as in Eq. (1b), and term d was determined through trial and error until the best fit was found ($d = -0.1$). It is interesting to see that radiation transport in an optically thick pyroCu core can be described by simple geometrical functions, whereby the first two terms characterizes how much downwelling or upwelling diffusion dominates over the other, whereas the other two terms characterize where we are in the transition between areas dominated by downwelling or upwelling diffusion. To gain a better understanding of radiation transport in a pyroCu, we next attempt to reproduce the basic radiation pattern observed by the CAR instrument using 1D and 3D radiative transfer simulations.

3.2. Monte Carlo simulation

We now explore the optical characteristics of pyroCu using 1D and 3D radiative transfer simulations using Monte Carlo technique (e.g. Marchuk et al., 1980). The Monte Carlo model is an appropriately modified version of the code used in several earlier studies, including Varnai and Marshak (2001), and was also tested in the Intercomparison of 3D Radiation Codes (I3RC) project (Cahalan

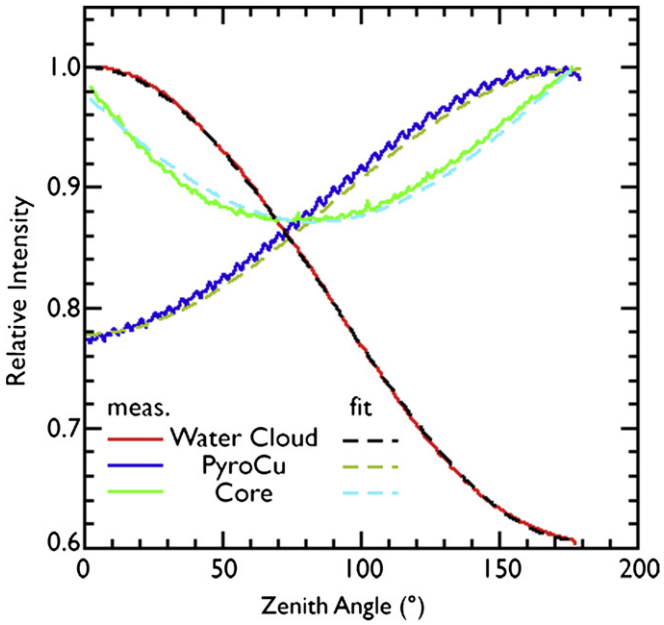

Fig. 5. Observed and fitted relative radiance at 0.472 μm represented by solid and dashed lines, respectively, for water cloud, pyroCu and the pyroCu core. The fitted lines for water cloud and pyroCu were generated by a cosine function given in Eq. (1b), with parameter "b" assuming a negative value for the pyroCu case. The pyroCu core was fitted by Eq. (2).

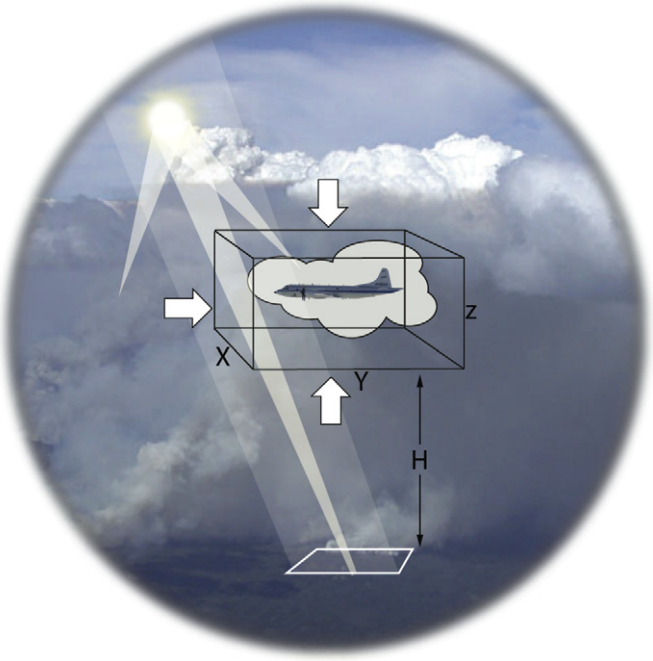

Fig. 6. Illustration of solar illumination paths responsible for the observed radiation patterns in Fig. 4a-c.

et al., 2005). The actual code used in this study was also tested through comparisons with DISORT (Discrete Ordinates Radiative Transfer) model (Stamnes et al., 1988) runs for absorbing, plane-parallel clouds. To keep simulation uncertainties below 0.5%, each result is based on 4 million photon trajectories in backward Monte Carlo simulations.

Because the purpose of these Monte Carlo simulations is to understand the basic behaviors in Fig. 4 (and not to simulate the exact values observed by CAR), the simulations use a simple setup (Fig. 6). The calculations assume a 2D slab cloud that is infinite in the cross-sun (Y) direction, lies between $H = 1$ km and $H = 2$ km altitudes, and is 1 km wide ($\Delta Z = \Delta X = 1$ km). The extinction coefficient is 100 km^{-1}, so the cloud optical thickness is 100 in both Z and X directions. Because we simulate radiances deep inside the cloud, where multiple scattering minimizes the details of the scattering phase function, we assume the cloud particles have a Henyey-Greenstein phase function with an asymmetry parameter of $g = 0.85$. The solar zenith angle is taken as 30° and the surface albedo as 0.2. For simplicity, no atmospheric effects—Rayleigh scattering or gaseous absorption—are considered.

Fig. 7 shows simulation results that can shed light onto the behaviors in Fig. 4a, b and c. (At this stage we do not attempt to simulate the complex behaviors in Fig. 4d.) The black dashed line displays a qualitatively similar behavior to the clean cloud in Fig. 4a and shows the general behavior of 1D radiation calculations, which assume horizontally homogeneous and infinite (plane-parallel) clouds. The line illustrates that in 1D cases, the radiance of the highly diffuse radiation deep inside clouds is always greater looking up than looking down regardless of the amount of particle absorption. This is because the conservation of energy and the lack of light sources below imply that the upwelling flux can never exceed the downwelling flux. This particular simulation was based on a single scattering albedo of 0.975, representing stronger absorption than typically occur in liquid water clouds in the visible to near-infrared (cf. Fig. 4a), but with a shape typical of what occurs in absorbing liquid water clouds.

The other three curves in Fig. 7 are from 3D simulations. Energy conservation requires the scene average net radiation to flow downward even in 3D situations. However, this trend can reverse locally inside clouds in 3D situations. In our simulations, this

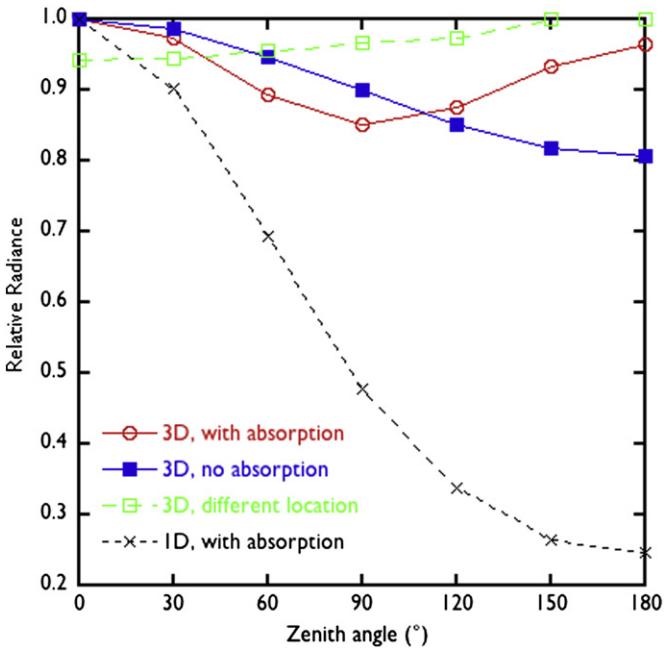

Fig. 7. Simulated CAR data used for understanding the observed behaviors in Fig. 4. The figure shows simulated CAR data for an azimuth perpendicular to the sun (90° relative azimuth). The black, red, and blue curves are for the horizontal center of the cloud at 1.4 km altitude. The green curve, simulating behaviors observed at a different (pyroCu) segment of the flight path, is for a point 200 m away from the sunlit cloud edge at 1.3 km altitude. All simulations with absorption were based on a single scattering albedo of 0.975, representing stronger absorption than typically occur in liquid water clouds in the visible to near-infrared.

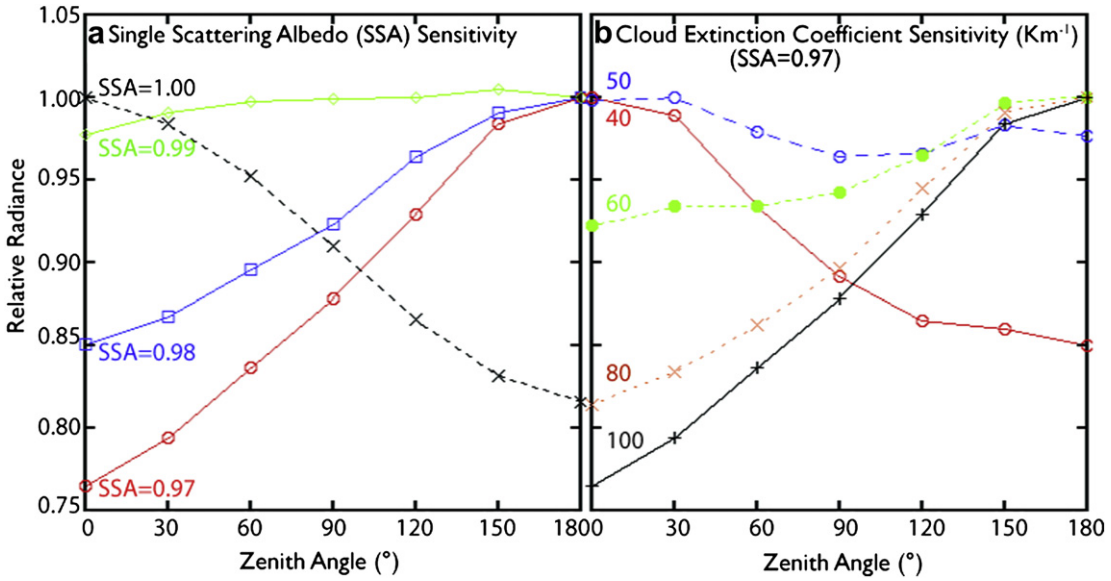

Fig. 8. Impact of (a) variations in single scattering albedo (SSA) at a constant cloud extinction coefficient (100 km^{-1}); and (b) variations in cloud extinction coefficient at a constant SSA (0.97). The simulations are for 85° relative azimuth at a point 300 m away from the sunlit cloud edge at 1.3 km altitude.

reversal occurs because large amounts of radiation can reach the surface easily in clear areas between clouds and, after reflection from the surface, can enter through the cloud base and create an upwelling flow of radiation inside the cloud. In addition, sunlight entering a sunlit cloud side can create a flow toward the shadowy side (Fig. 6), and the flow can have an upward component if most of this sunlight enters the cloud side below the aircraft. Although not considered in our simple demonstrative simulations, in real situations scattering by air molecules, aerosols, and low-level clouds can also cause sunlight to enter a pyroCu through its base or through the lower portions of cloud sides.

The blue squares in Fig. 7 show that the downward flow entering through the cloud top still dominates our 3D case if there is no absorption. The red circles, however, show that absorption can drastically change the radiation pattern by depleting much of the downwelling radiation wending its way through the cloud. As a result, the upwelling flow of radiation reflected from the surface can match the weakened downwelling flow, creating comparable radiance peaks looking up ($\theta = 0°$) and down ($\theta = 180°$). This is similar to the behavior in Fig. 4c (pyroCu core). Lastly, the green dashed curve in Fig. 7 shows that for a lower altitude cloud, absorption reduces the downwelling (upwelling) radiation more (less), and so upwelling radiation can fully dominate and create a trend similar to that in Fig. 4b (pyroCu).

Finally, Fig. 8 more explicitly explores the role of absorption and scattering properties in shaping radiation patterns. Fig. 8a shows that even relatively weak absorption (SSA $\leq$ 0.99) can allow upwelling radiation to match or even exceed the downwelling flow in a 3D situation. The figure also suggests that spectral changes in single scattering albedo (e.g., Fig. 9b in Eck et al., 2009) may also play a role in shaping the details of our observations. In turn, Fig. 8b shows that increasing the number of particles (i.e., the extinction coefficient) yields similar effects to increasing their absorptivity, as both changes make it harder for radiation to reach an instrument deep inside the cloud. This implies that radiation patterns similar to those observed in pyroCu and pyroCu core (Fig. 4b and c) can arise in thick clouds even if absorption is relatively weak, although stronger absorption is required in thin clouds. The interplay between scattering and absorption can also allow upwelling radiation to dominate even in the upper parts of clouds if particles are distributed unevenly. For example, if the cloud extinction coefficient increases with altitude (e.g., Raga and Jonas, 1993)—e.g., as ascending droplets grow through condensation—strong absorption or scattering above can greatly reduce the downwelling radiation and allow the upwelling radiation reflected from the ground to dominate even at high altitudes.

4. Conclusions

This study provides an analysis of airborne radiation measurements with the CAR instrument within strong pyroCu over boreal forest fires in Saskatchewan, Canada during the Arctic Research of the Composition of the Troposphere from Aircraft and Satellites (ARCTAS) summer field campaign in 2008.

We found the pyroCu core to be very interesting having very low light levels from the UV to near IR regions of the electromagnetic spectrum, and very uniform radiance field in all directions. Spectral radiances measured within the core were very small <1 Wm^{-2} μm^{-1} sr^{-1} in the ultraviolet and visible bands, $\lambda < 0.5$ μm, and at $\lambda = 1.6$ μm, but substantially larger (2–5 Wm^{-2} μm^{-1} sr^{-1}) for 0.5 μm $< \lambda <$ 1.3 μm, independent of direction. We found the angular distribution of radiance within the pyroCu to be related to the diffusion domain in liquid water clouds that can be described by very similar geometrical functions with a few additional terms. We conclude that radiation transport in an optically thick pyroCu can be described by simple geometrical functions, whereby the first two terms characterizes how much downwelling or upwelling diffusion dominates over the other, whereas the other two terms characterize where we are in the transition between areas dominated by downwelling or upwelling diffusion. We demonstrate with Monte Carlo simulation that radiation transport in pyroCu is inherently a 3D problem and must account for strong particle absorption or particle extinction coefficients. The proposed simple description of the radiation distribution within the pyroCu or pyroCu core may lead to better understanding of these cloud systems and provide a simpler solution for their inclusion in cloud resolving models.

Acknowledgments

This research was supported by the Science Mission Directorate of the National Aeronautics and Space Administration (NASA) as part of the Radiation Sciences Program under Hal B. Maring and Airborne Science Program under Bruce Tagg. We thank NASA P-3 crew members, and also the following individuals (R. Kahn, R. A. Marshak, R. Cahalan, W. Wiscombe, F. Ewald, A. Nenes, and T. Lathem) for insightful discussions and comments. We also thank the editor and two anonymous reviewers for their valuable comments. This work was performed under NASA Grants NNX08A89G and NNX11AQ98G.

References

Andreae, M.O., Rosenfeld, D., Artaxo, P., Costa, A.A., Frank, G.P., Longo, K.M., Silva-Dias, M.A.F., 2004. Smoking rain clouds over the Amazon. Science 303, 1337. doi:10.1126/science.1092779.

Barrick, J.D., Aknan, A.A., 2008. P-3B Supporting Measurements Data System (PDS). http://www.espo.nasa.gov/arctas/docs/instruments/pds.pdf.

Cahalan, R.F., Oreopoulos, L., Marshak, A., Evans, K.F., Davis, A., Pincus, R., Yetzer, K., Mayer, B., Davies, R., Ackerman, T., Barker, H., Clothiaux, E., Ellingson, R., Garay, M., Kassianov, E., Kinne, S., Macke, A., OHirok, W., Partain, P., Prigarin, S., Rublev, A., Stephens, G., Szczap, F., Takara, E., Várnai, T., Wen, G., Zhuravleva, T., 2005. The international intercomparison of 3D radiation codes (I3RC): bringing together the most advanced radiative transfer tools for cloudy atmospheres. Bull. Amer. Meteor. Soc. 86, 1275–1293.

Calle, A., Casanova, J.L., Gonzalez-Alonso, F., 2009. Impact of point spread function of msg-seviri on active fire detection. Int. J. Remote Sens. 30, 4567–4579.

Clarke, A., McNaughton, C., Kapustin, V., Shinozuka, Y., Howell, S., Dibb, J., Zhou, J., Anderson, B., Brekhovskikh, V., Turner, H., Pinkerton, M., 2007. Biomass burning and pollution aerosol over North America: organic components and their influence on spectral optical properties and humidification response. J. Geophys. Res. 112, D12S18. doi:10.1029/2006JD007777.

Csiszar, I.A., Morisette, J.T., Giglio, L., 2006. Validation of active fire detection from moderate-resolution satellite sensors: the MODIS example in northern Eurasia. IEEE Trans. Geosci. Remote Sens. 44, 1757–1764.

Damoah, R., Spichtinger, N., Servranckx, R., Fromm, M., Eloranta, E.W., Razenkov, I.A., James, P., Shulski, M., Forster, C., Stohl, A., 2006. A case study of pyro-convection using transport model and remote sensing data. Atmos. Chem. Phys. 6, 173–185.

Donnell, E.A., Fish, D.J., Dicks, E.M., 2001. Mechanisms for pollutant transport between the boundary layer and the free troposphere. J. Geophys. Res. 106, 7847–7856.

Eck, T.F., et al., 2009. Optical properties of boreal region biomass burning aerosols in central Alaska and seasonal variation of aerosol optical depth at an Arctic coastal site. J. Geophys. Res. 114, D11201. doi:10.1029/2008JD010870.

Fromm, M., Servranckx, R., 2003. Transport of forest fire smoke above the tropopause by supercell convection. Geophys. Res. Lett. 30, 1542. doi:10.1029/2002GL016820.

Fromm, M., Bevilacqua, R., Servranckx, R., Rosen, J., Thayer, J., Herman, J., Larko, D., Servranckx, R., 2005. Pyro-cumulonimbus injection of smoke to the stratosphere: observations and impact of a super blowup in northwestern Canada on 3–4 August 1998. J. Geophys. Res. 110, D08205. doi:10.1029/2004JD005350.

Fromm, M., Lindsey, D.T., Servranckx, R., Yue, G., Trickl, T., Sica, R., Doucet, P., Godin-Beekmann, S., 2010. The untold story of pyrocumulonimbus. Bull. Ameri. Meteor. Soc. 91, 1193–1209.

Gatebe, C.K., King, M.D., Platnick, S., Arnold, G.T., Vermote, E.F., Schmid, B., 2003. Airborne spectral measurements of surface-atmosphere anisotropy for several surfaces and ecosystems over southern Africa. J. Geophys. Res. 108, 8489. doi:10.1029/2002JD002397.

Giglio, L., Descloitres, J., Justice, C., Kaufman, Y., 2003. An enhanced contextual fire detection algorithm for MODIS. Remote Sens. Environ. 87, 273–282.

Howell, S.G., Clarke, A.D., Shinozuka, Y., Kapustin, V., McNaughton, C.S., Huebert, B.J., Doherty, S.J., Anderson, T.L., 2006. Influence of relative humidity upon pollution and dust during ACE-Asia: size distributions and implications for optical properties. J. Geophys. Res. 111, D06205. doi:10.1029/2004JD005759.

Ichoku, C., Giglio, L., Wooster, M.J., Remer, L.A., 2008. Global characterization of biomass-burning patterns using satellite measurements of fire radiative energy. Remote Sens. Environ. 112, 2950–2962.

Jacob, D.J., Crawford, J.H., Maring, H., Clarke, A.D., Dibb, J.E., Emmons, L.K., Ferrare, R.A., Hostetler, C.A., Russell, P.B., Singh, H.B., Thompson, A.M., Shaw, G.E., McCauley, E., Pederson, J.R., Fisher, J.A., 2010. The Arctic research of the composition of the troposphere from aircraft and satellites (ARCTAS) mission: design, execution, and first results. Atmos. Chem. Phys. 10, 5191–5212.

Kahn, R.A., Chen, Y., Nelson, D.L., Leung, F.Y., Li, Q.B., Diner, D.J., Logan, J.A., 2008. Wildfire smoke injection heights: two perspectives from space. Geophys. Res. Lett. 35, L04809. doi:10.1029/2007GL032165.

King, M.D., 1981. A method for determining the single scattering albedo of clouds through observation of the internal scattered radiation field. J. Atmos. Sci. 38, 2031–2044.

King, M.D., Strange, M.G., Leone, P., Blaine, L.R., 1986. Multiwavelength scanning radiometer for airborne measurements of scattered radiation within clouds. J. Atmos. Oceanic Technol. 3, 513–522.

King, M.D., Radke, L.F., Hobbs, P.V., 1990. Determination of the spectral absorption of solar radiation by marine stratocumulus clouds from airborne measurements within clouds. J. Atmos. Sci. 47, 894–907.

Lance, S., Medina, J., Smith, J.N., Nenes, A., 2006. Mapping the operation of the DMT continuous flow CCN counter. Aerosol Sci. Technol. 40, 242–254.

Luderer, G., Trentmann, J., Winterrath, T., Textor, C., Herzog, M., Graf, H.-F., Andreae, M.O., 2006. Modeling of biomass smoke injection into the lower stratosphere (part II): sensitivity studies. Atmos. Chem. Phys. 6, 5261–5277.

Marchuk, G.I., Mikhailov, G.A., Nazaraliev, M.A., Darbinjan, R.A., Kargin, B.A., Elepov, B.S., 1980. The Monte Carlo Methods in Atmospheric Optics. Springer-Verlag, pp. 208.

McCarter, R.J., Broido, A., 1965. Radiative and convective energy from wood crib fires. Pyrodyn. 2, 65–85.

Packham, D.R., 1969. Heat transfer above a small ground fire. Aust. For. Res. 5, 19–24.

Pilewskie, P., Pommier, J., Bergstrom, R., Gore, W., Howard, S., Rabbette, M., Schmid, B., Hobbs, P.V., Tsay, S.C., 2003. Solar spectral radiative forcing during the Southern African regional science initiative. J. Geophys. Res. 108, 8486. doi:10.1029/2002JD002411.

Polonsky, I.N., Davis, A.B., 2004. Lateral photon transport in dense scattering and weakly absorbing media of finite thickness: asymptotic analysis of the space–time Green function. J. Opt. Soc. Am. A. 21, 1018–1025.

Provencal, R., Gupta, M., Owano, T.G., Baer, D.S., Ricci, K.N., O'Keefe, A., Podolske, J.R., 2005. Cavity-enhanced quantum-cascade laser-based instrument for carbon monoxide measurements. Appl. Opt. 44, 6712–6717.

Raga, G.B., Jonas, P.R., 1993. Microphysical and radiative properties of small cumulus clouds over the sea. Quart. J. Royal Meteor. Soc. 119, 1399–1417.

Roberts, G., Nenes, A., 2005. A continuous-flow streamwise thermal-gradient CCN chamber for atmospheric measurements. Aerosol Sci. Technol. 39, 206–221.

Rosenfeld, D., Fromm, M., Trentmann, J., Luderer, G., Andreae, M.O., Servranckx, R., 2007. The Chisholm firestorm: observed microstructure, precipitation and lightning activity of a pyro-cumulonimbus. Atmos. Chem. Phys. 7, 645–659.

Russell, P.B., Livingston, J.M., Hignett, P., Kinne, S., Wong, J., Hobbs, P.V., 1999. Aerosol-induced radiative flux changes off the United States Mid-Atlantic coast: comparison of values calculated from sunphotometer and in situ data with those measured by airborne pyranometer. J. Geophys. Res. 104, 2289–2307.

Shinozuka, Y., Redemann, J., Livingston, J.M., Russell, P.B., Clarke, A.D., Howell, S.G., Freitag, S., O'Neill, N.T., Reid, E.A., Johnson, R., Ramachandran, S., McNaughton, C.S., Kapustin, V.N., Brekhovskikh, V., Holben, B.N., McArthur, L.J.B., 2011. Airborne observation of aerosol optical depth during ARCTAS: vertical profiles, inter-comparison and fine-mode fraction. Atmos. Chem. Phys. 11, 3673–3688.

Soja, A.J., Tchebakova, N.M., French, N.H.F., Flannigan, M.D., Shugart, H.H., Stocks, B.J., Sukhinin, A.I., Parfenova, E.I., Chapin, F.S., Stackhouse, P.W., 2007. Climate-induced boreal forest change: predictions versus current observations. Glob. Planet. Change 56, 274–296.

Stamnes, K., Tsay, S.-C., Wiscombe, W., Jayaweera, K., 1988. Numerically stable algorithm for discrete-ordinate-method radiative transfer in multiple scattering and emitting layered media. Appl. Opt. 27, 2502–2509.

Stocks, B.J., Mason, J.A., Todd, J.B., Bosch, E.M., Wotton, B.M., Amiro, B.D., Flannigan, M.D., Hirsch, K.G., Logan, K.A., Martell, D.L., Skinner, W.R., 2003. Large forest fires in Canada, 1959–1997. J. Geophys. Res. 108, 8149. doi:10.1029/2001JD000484.

Strawa, A.W., Provencal, R., Owano, T., Kirschstetter, T.W., Hallar, G., Williams, M.B., 2007. Aero3X: Fast, Accurate Measurement of Aerosol Optical Properties for Climate and Air Quality Studies. American Geophysical Union. Fall Meeting 2007, abstract #A53G-03. http://adsabs.harvard.edu/abs/2007AGUFM.A53G.03S.

Trentmann, J., Luderer, G., Winterrath, T., Fromm, M., Servranckx, R., Textor, C., Herzog, M., Andreae, M.O., 2006. Modeling of biomass smoke injection into the lower stratosphere by a large forest fire (Part I): reference study. Atmos. Chem. Phys. 6, 5247–5260.

Val Martin, M., Logan, J.A., Kahn, R.A., Leung, F.-Y., Nelson, D.L., Diner, D.J., 2010. Smoke injection heights from fires in North America: analysis of 5 years of satellite observations. Atmos. Chem. Phys. 10, 1491–1510.

Varnai, T., Marshak, A., 2001. Statistical analysis of the uncertainties in cloud optical depth retrievals caused by three-dimensional radiative effects. J. Atmos. Sci. 58, 1540–1548.

Wooster, M.J., 2002. Small-scale experimental testing of fire radiative energy for quantifying mass combusted in natural vegetation fires. Geophys. Res. Lett. 29. doi:10.1029/2002GL015487.

Wooster, M.J., Roberts, G., Perry, G.L.W., Kaufman, Y.J., 2005. Retrieval of biomass combustion rates and totals from fire radiative power observations: FRP derivation and calibration relationships between biomass consumption and fire radiative energy release. J. Geophys. Res. 110, D24311. doi:10.1029/2005JD006318.